Check for updates

Sol-gel synthesis of magnesium aluminate and synergistic degradation of Cr(VI) ion by adsorption and photocatalysis

Miao Liu[1]*, Yi Wang[1], Yingjun Wu[1], Chunyang Liu[2] and Xin Liu[3]

[1]College of New Energy and Environment, Jilin University, Changchun, China, [2]Changchun Ecological and Environmental Monitoring Centre of Jilin Province, Changchun, China, [3]Changchun Institute of Technology, Changchun, China

Introduction: Magnesium aluminate ($MgAl_2O_4$) is a new adsorbent, which can be used to adsorb dyes and drugs, but it has not been used to adsorb Cr(VI) ions.

Methods: A conventional polyacrylamide gel route with the different chelating agents including ethylenediamine tetraacetic acid (EDTA), oxalic acid and salicylic acid have been applied to synthesis the $MgAl_2O_4$ nanoparticles with the high adsorption capacity and photocatalytic reduction capacity for the adsorption and reduction of Cr(VI). The phase compositions, microstructure characteristics, optical properties, adsorption capacities and photocatalytic reduction capacities of $MgAl_2O_4$ nanoparticles can be effectively regulated by changing the type of chelating agent.

Results and discussion: The pure phase $MgAl_2O_4$ nanoparticles were obtained by using EDTA and oxalic acid as chelating agents, but a small amount of MgO impurity appeared in the $MgAl_2O_4$ nanoparticles obtained by salicylic acid as chelating agents, which inhibited the adsorption and photocatalytic reduction ability of $MgAl_2O_4$ nanoparticles. The optimal $MgAl_2O_4$ content, Cr(VI) initial concentration and pH value were 0.75 mg/L, 100 mg/L and 5, respectively. The photocatalytic reduction capacity of $MgAl_2O_4$ nanoparticles obtained by oxalic acid as chelating agents was 3.56 times that of $MgAl_2O_4$ nanoparticles obtained by salicylic acid as chelating agents. The high adsorption capacity of $MgAl_2O_4$ nanoparticles is mainly due to electrostatic adsorption, while the high photocatalytic reduction capacity is mainly due to the high reduction capacity of active free radicals generated by the conduction electrons and valence band holes of $MgAl_2O_4$ nanoparticles.

KEYWORDS
chelating agents, $MgAl_2O_4$, oxalic acid, adsorption, reduction capacity

1 Introduction

Chromium is a heavy metal ion commonly found in the smelting, painting and electroplating industries, with high mobility and toxicity, and Cr ions are often detected in wastewater. (Budiana et al., 2021; Kumar et al., 2022). In nature, chromium mainly contains two valence states, Cr(VI) and Cr(III). Cr(VI) usually has higher toxicity and mobility than Cr(III), is easy to gather in the roots of plants, and exists in wastewater, which will bring great harm to human production and life. (Fan et al., 2021; Uddin et al., 2021).

Therefore, the reduction of Cr(VI) to Cr(III) can greatly reduce the pollution of chromium to the environment, thereby reducing its harm to human health.

Recently, the main technical means to reduce Cr(VI) ion pollution in water environment including membrane separation, chemical reduction, ion exchange, adsorption and photocatalysis. (Kong et al., 2021a; Li et al., 2021; Liu et al., 2021). Among these methods, adsorption and photocatalysis are two effective means often used to reduce Cr(VI) ions, especially the photocatalysis technology driven by light energy is known as a green technology. (Zhang et al., 2021; Liu et al., 2022; Gao et al., 2022; Zhang et al., 2022). The development of semiconductor materials with the ability of adsorption and photocatalytic reduction has become one of the hot research topics in reducing Cr(VI) to Cr(III). (Li et al., 2021; Tripathy et al., 2022). Magnesium aluminate ($MgAl_2O_4$) is a kind of semiconductor material, which has been widely used in adsorption and photocatalytic degradation of organic dyes and drugs. (Muneeb et al., 2016; Mukherjee et al., 2020; Salmasi et al., 2022). It is well known that the physical and chemical properties of $MgAl_2O_4$ are strongly dependent on its morphology, surface defects and interface effects. The morphology, surface defects and interface effects of $MgAl_2O_4$ are mainly dependent on special synthesis methods.

To develop $MgAl_2O_4$ semiconductor materials with the ability of adsorption and photocatalysis, a new polyacrylamide gel method has been favored by researchers. (Hassanzadeh-Tabrizi, 2011; Liu et al., 2022). The $MgAl_2O_4$ semiconductor materials with different particle sizes can be synthesized by changing the experimental conditions such as the type of metal salt, the content of various additives, the reaction temperature and the type of chelating agent. However, the synthesis of $MgAl_2O_4$ nanoparticles with controllable size by different types of chelating agents has not been reported. Simultaneously, $MgAl_2O_4$ semiconductor materials have not been used to adsorption and photocatalytic reduction Cr(VI) to Cr(III). Therefore, it is of great significance to select a suitable chelating agent to synthesize $MgAl_2O_4$ nanoparticles and study the synergistic effect of adsorption and photocatalysis to reduce Cr(VI) ions.

In this paper, we propose the synthesis of three different $MgAl_2O_4$ nanoparticles using the polyacrylamide gel method and ethylenediamine tetraacetic acid (EDTA), oxalic acid and salicylic acid as chelating agents. The structure information, microstructure characteristics, optical properties, adsorption capacity and photocatalytic reduction capacity of $MgAl_2O_4$ nanoparticles were investigated by multiple characterization equipments. The $MgAl_2O_4$ nanoparticles were used to adsorption and photocatalytic reduction of Cr(VI) ions for the first time. The effects of different experimental parameters, including Cr(VI) initial concentration, $MgAl_2O_4$ content, pH value, adsorption time and reaction temperature on the adsorption capacity of $MgAl_2O_4$ nanoparticles were explored in detail. Combining adsorption experiment, photocatalysis experiment and energy band theory, a reasonable adsorption and photocatalysis mechanism is proposed.

2 Experimental section

2.1 Preparation of $MgAl_2O_4$ nanoparticles

To study the effects of different chelating agents on the structure, morphology and physicochemical properties of $MgAl_2O_4$ nanoparticles, ethylenediamine tetraacetic acid (EDTA), oxalic acid and salicylic acid

were selected as chelating agents. A certain mass of aluminium trichloride ($AlCl_3$), magnesium chloride hexahydrate ($MgCl_2 \cdot 9H_2O$) is weighed on the basis of the molar ratio of $n_{Mg} : n_{Al} = 1 : 2$. Meanwhile, a chelating agent with a molar ratio of 5:1 to metal ions, 20 g glucose, 9.5958 g acrylamide and 1.9192 g methylene bisacrylamide were weighed. The reagents were successively dissolved in 100 mL deionized water, and after all the reagents were completely dissolved, the temperature was raised to 90°C to form a jelly-like gel. Subsequently, the jelly-like gel was transferred to a drying oven to dry at 120°C for 24 h to obtain a black xerogel. The $MgAl_2O_4$ nanoparticles were obtained by smashing the dry gel and sintering it in a box furnace at 800°C for 10 h. The $MgAl_2O_4$ nanoparticles prepared by selecting EDTA, oxalic acid and salicylic acid as chelating agents were labeled as samples S1, S2 and S3, respectively. The preparation flow chart of $MgAl_2O_4$ nanoparticles as depicted in Figure 1.
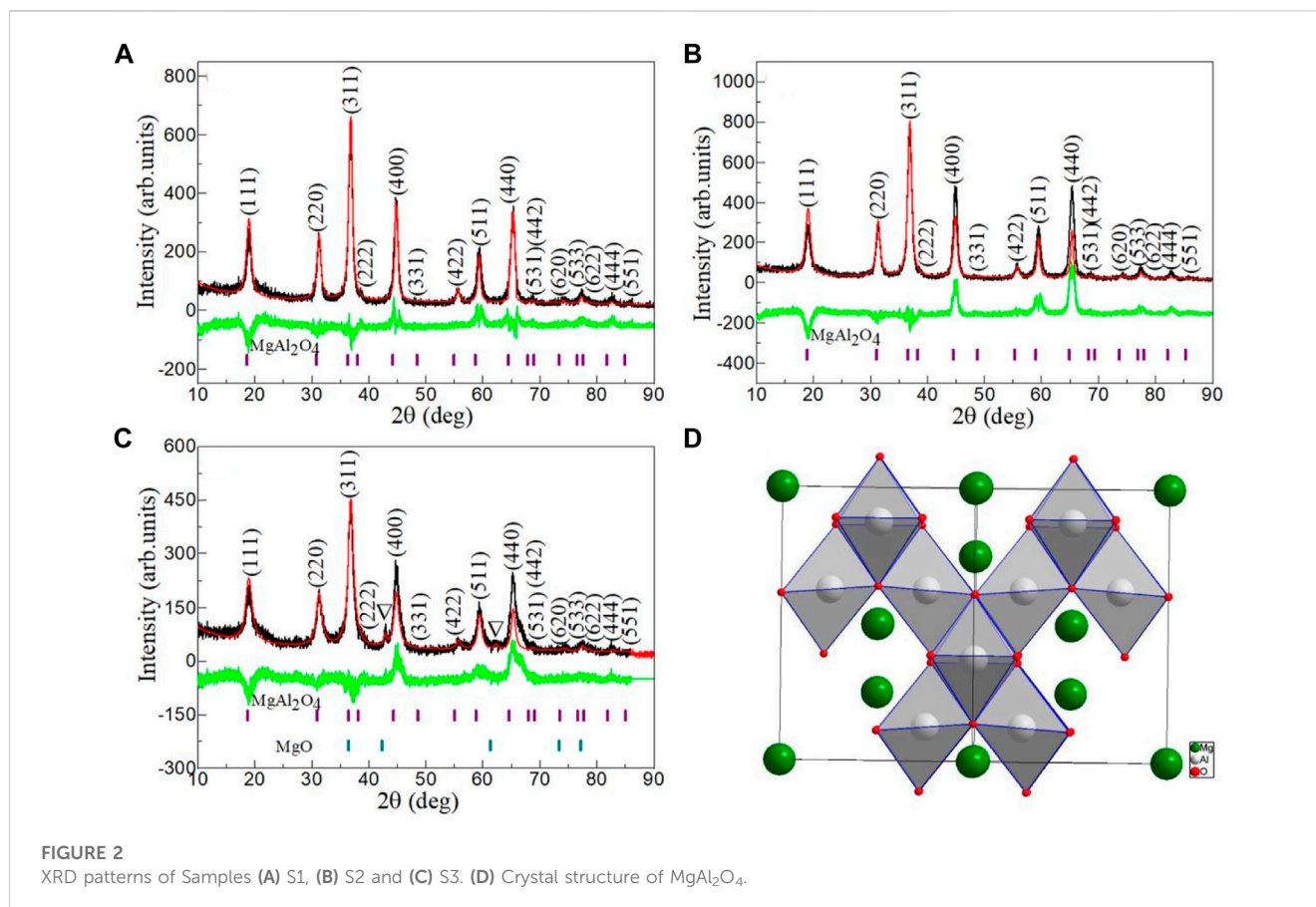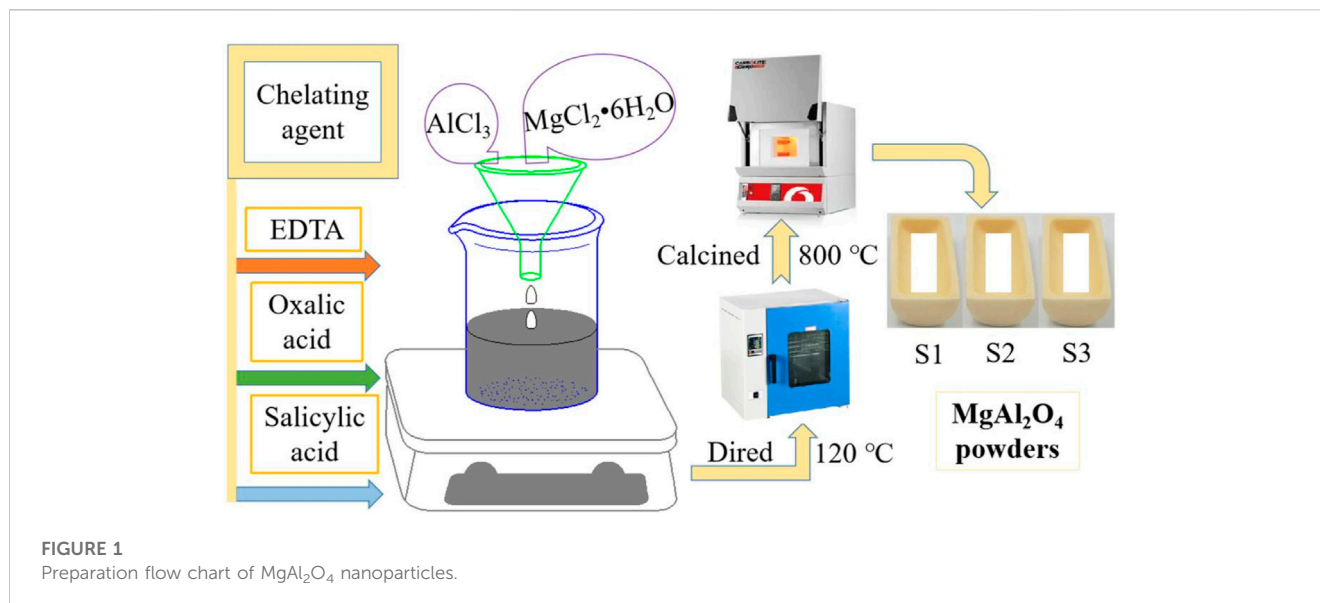
2.2 Material characterization

The phase information of $MgAl_2O_4$ nanoparticles was characterized by the means of D8 ADVANCE (Bruker Germany) X-ray powder diffraction (XRD) with the Cu Kα radiation at a X-ray wavelength of 1.5406 Å and operated at an accelerating voltage of 30 kV and accelerating current of 20 mA. The morphological characteristics of $MgAl_2O_4$ nanoparticles were observed by a Hitachi S-4800 cold-field emission scanning electron microscope (FE-SEM) with the accelerating voltage of 20 kV and a JEOL JEM-2100F transmission electron microscope (TEM) operated at an accelerating voltage of 5 kV and high-resolution TEM (HRTEM) operated at 300 kV. Ultraviolet-visible (UV-vis) absorption spectra of $MgAl_2O_4$ nanoparticles were characterized by a TU-1901 UV-visible spectrophotometer on the basis of the $BaSO_4$ used as reference and the test wavelength range of 200–850 nm.

2.3 Adsorption experiments

To perform the adsorption experiments, K_2CrO_4 solution was used as an ion source for Cr(VI). The adsorbent content, initial concentration of Cr(VI), pH value, adsorption time and reaction temperature were 0.25–1 g/L, 50–200 mg/L, 3–13, 180 min, and 283–313 K, respectively. According to the above experimental conditions, Cr(VI) solution of the corresponding concentration was configured, and $MgAl_2O_4$ nanoparticles of the corresponding adsorption content were added, and the magnetic stirrer kept stirring. For the first 30 min of adsorption, the solution is taken every 5 min, and then the sample is taken every half hour. Subsequently, the concentration of Cr(VI) was measured by a dinitrodiphenyl carbazide spectrophotometric method. (Milačič et al., 1992). The amount of Cr(VI) ions adsorbed by the $MgAl_2O_4$ nanoparticles was calculated from the Equation 1.

$$q = \frac{(C_0 - C_t) \times V}{m_{Adsorbent}} \qquad (1)$$

Where, q is the amount adsorbed (mg/g) of Cr(VI) ions, C_0 is the Cr(VI) initial concentration (mg/L), C_t is the concentration at time t of Cr(VI) ions, V is the volume, and $m_{Adsorbent}$ are the mass of adsorbent (g).

FIGURE 1
Preparation flow chart of MgAl$_2$O$_4$ nanoparticles.

FIGURE 2
XRD patterns of Samples **(A)** S1, **(B)** S2 and **(C)** S3. **(D)** Crystal structure of MgAl$_2$O$_4$.

2.4 Photocatalytic experiments

The photocatalytic reduction ability of MgAl$_2$O$_4$ nanoparticles was studied by exposing the reaction solution after adsorption equilibrium to xenon lamp light source which can emit simulated sunlight for 1 h. The sample is taken every 10 minutes, and the concentration of the obtained solution is also determined by the above dinitrodiphenyl carbazide spectrophotometric method. The catalyst content, initial concentration of Cr(VI), pH value, illumination time and reaction temperature were 0.75 g/L, 100 mg/L, 5, 60 min, and 283 K, respectively. The degradation percentage (DP%) of MgAl$_2$O$_4$ nanoparticles can be estimated by Equation 2.
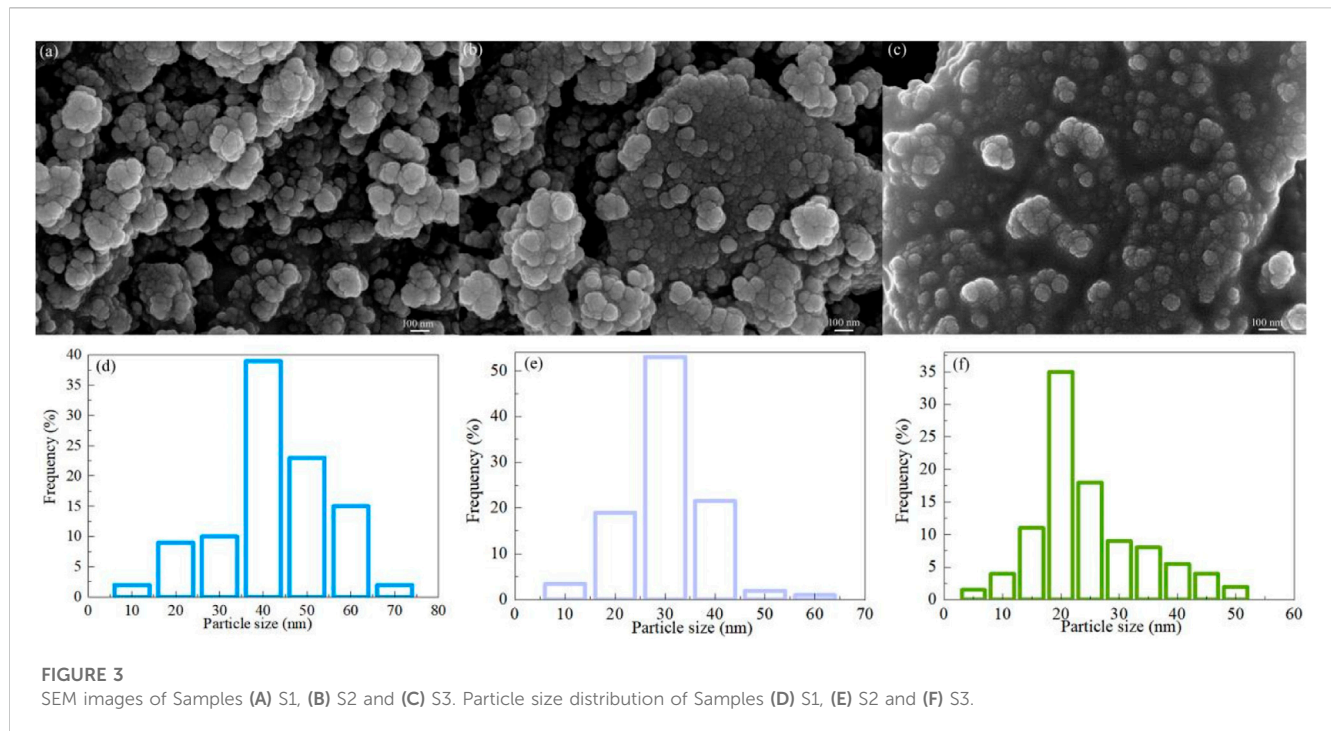
FIGURE 3
SEM images of Samples **(A)** S1, **(B)** S2 and **(C)** S3. Particle size distribution of Samples **(D)** S1, **(E)** S2 and **(F)** S3.

$$DP\% = \left(1 - \frac{C_t}{C_o}\right) \times 100\% \qquad (2)$$

3 Results and discussions

3.1 Phase and crystal structure

The phase structure and purity of semiconductor materials can be characterized by XRD. Figures 2A–C depicts the XRD patterns of Samples S1, S2 and S3. For the Samples S1 and S2, all diffraction peaks can be attributed to the cubic spinel $MgAl_2O_4$ with the standard Joint committee on powder diffraction Standards (JCPDS) card No. 84–0377. However, in addition to the diffraction peaks of $MgAl_2O_4$, the Sample S3 also contains a small amount of cubic phase MgO with the standard JCPDS card No. 79–0612. The results show that the pure $MgAl_2O_4$ can be obtained when EDTA and oxalic acid are used as chelating agents, but the impurity phase of MgO appears when salicylic acid is used as chelating agents to prepare $MgAl_2O_4$. This result is mainly related to the coordination number of $MgAl_2O_4$ and the coordination ability of the chelating agent. (Luan et al., 2006; Ganesh, 2013; Rahmat et al., 2018). Based on the Scherrer Equation 3 and the (311), (400) and (440) diffraction peaks, the mean crystallite size (D) of Samples S1, S2, and S3 can be estimated.

$$DP = \frac{k\lambda}{\beta \cos \theta} \qquad (3)$$

Where, k = 0.9 is the shape factor, β is the full-width at half maximum, λ is the X-ray wavelength and θ is the diffraction angle. The average crystallite sizes of samples S1, S2, and S3 were calculated to be 38, 27, and 21 nm, respectively. Figure 2D displays the crystal structure of $MgAl_2O_4$. In the crystal structure, oxygen ions are packed cubic tightly, magnesium ions are filled in one-eighth of the tetrahedral space, and aluminum ions are filled in one-half of the octahedral space.

3.2 Surface micro-structure

The microstructure of semiconductor material has great influence on its physical and chemical properties. The surface microstructure of $MgAl_2O_4$ can be characterized by SEM and TEM. Figures 3A–C shows the SEM images of Samples S1, S2 and S3. The $MgAl_2O_4$ particles obtained by different chelating agents are approximately spherical, and the particles are fine and the agglomeration is obvious. The different chelating agents only affect the particle size and agglomeration degree of $MgAl_2O_4$ nanoparticles, but do not affect its shape. Figures 3D–F displays the particle size distribution of Samples S1, S2 and S3. The mean particle sizes of Samples S1, S2 and S3 are 40, 30 and 20 nm, respectively. The particle size of $MgAl_2O_4$ observed by SEM is basically consistent with that calculated by XRD. The main reason for the different size of $MgAl_2O_4$ nanoparticles obtained by different chelating agents is that $MgAl_2O_4$ has different crystal growth laws due to different chelating ability of chelating agents.

Figures 4A, B displays the TEM images of Samples S1 and S2. This result is similar to that observed by SEM, the $MgAl_2O_4$ nanoparticles are approximately spherical, and the agglomeration between particles is obvious. Figures 4C, D shows the HRTEM images of Samples S1 and S2. For the Sample S1, the lattice spacing of 0.28, 0.24, 0.20 and 0.14 nm corresponds to the d-spacing of (220), (311), (400) and (440) planes with the cubic $MgAl_2O_4$, respectively. For the Sample S2, the lattice spacing of 0.28 and 0.24 nm corresponds to the d-spacing of (220) and (311) planes with the cubic $MgAl_2O_4$, respectively. These results confirmed the absence of other impurities in Samples S1 and S2.
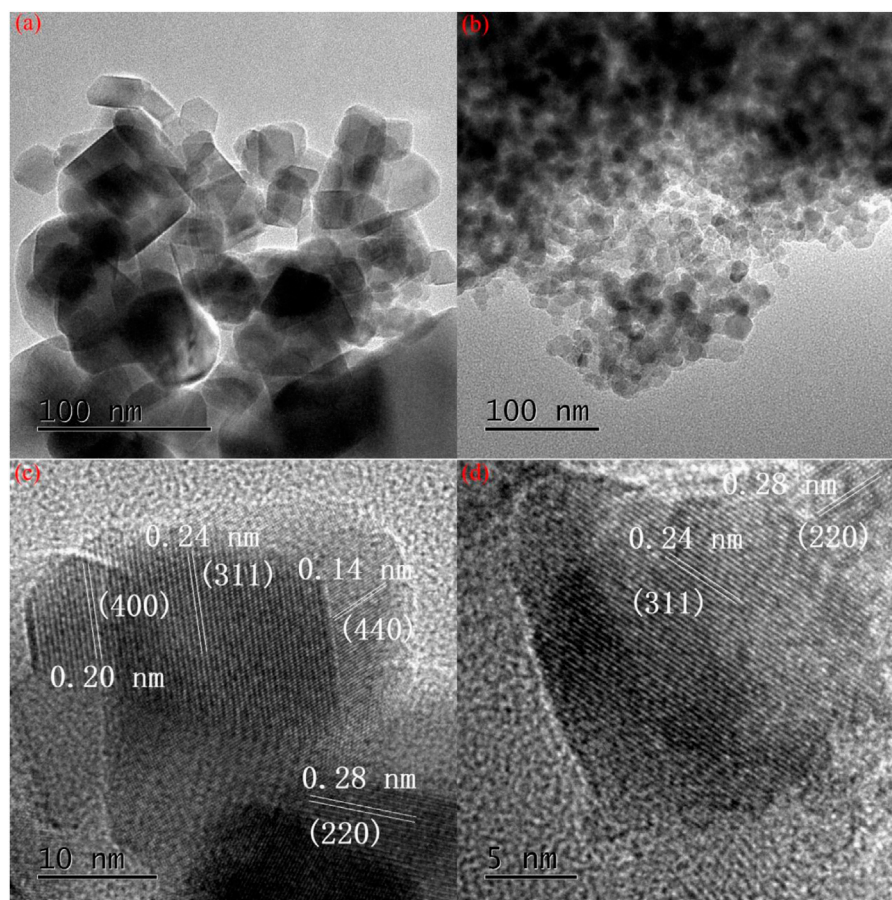
FIGURE 4
TEM images of Samples **(A)** S1 and **(B)** S2. HRTEM images of Samples **(C)** S1 and **(D)** S2.
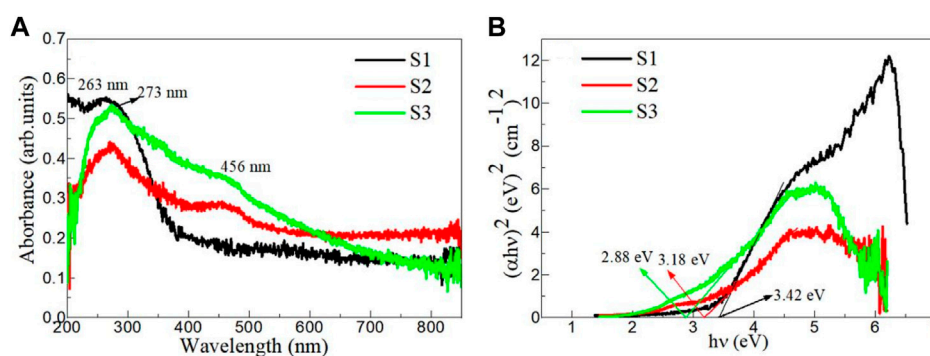

FIGURE 5
(A) UV-Vis absorption spectra and **(B)** Tauc's plots of Samples S1, S2 and S3.

3.3 Optical properties

The ultraviolet-visible absorption spectra of semiconductor materials can probe into whether the semiconductor materials can respond to visible light, and then guide the selection of light sources for photocatalysis experiments. Figure 5A shows the UV-

Vis absorption spectra of Samples S1, S2 and S3. For the Sample S1, the optical absorption coefficient decreases with the increasing of wavelength. A significant absorption peak was observed at 263 nm, mainly due to the anion vacancy F^+ center in $MgAl_2O_4$. (Nassar et al., 2014). The results show that the Sample S1 has a high UV absorption coefficient, suggesting
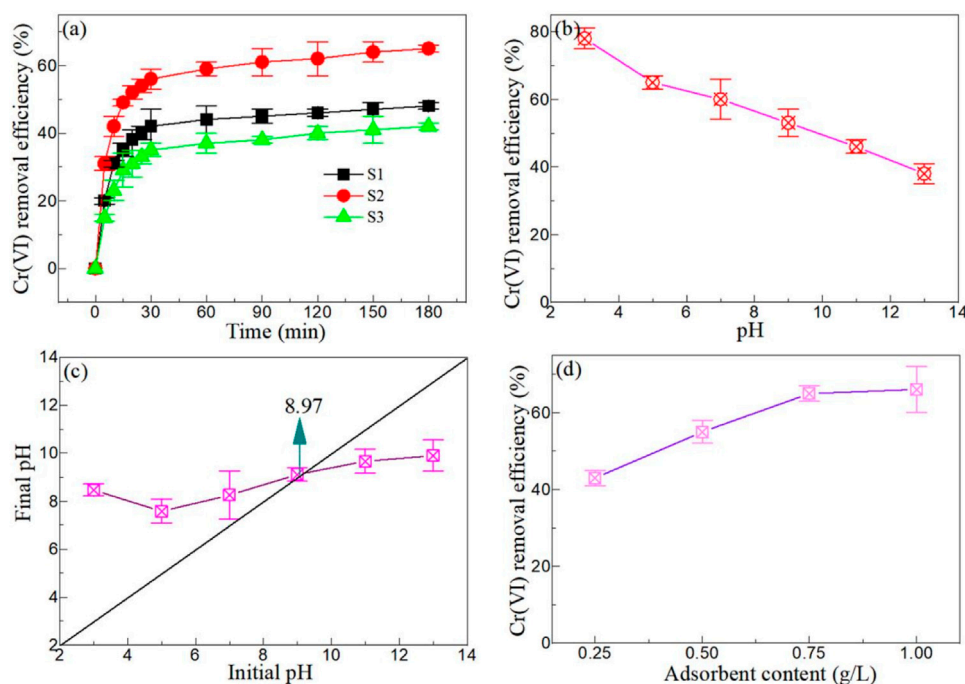
FIGURE 6
(A) Effect of adsorption time on the adsorption capacities of Cr(VI) by Samples S1, S2, and S3 (C$_{Adsorbent}$ = 0.75 g/L, C$_{Cr(VI)}$ = 100 mg/L, pH = 5, and T = 283 K). **(B)** Effect of pH value on the adsorption capacities of Cr(VI) by Samples S2 (C$_{Adsorbent}$ = 0.75 g/L, C$_{Cr(VI)}$ = 100 mg/L, and T = 283 K). **(C)** A function of the initial pH and the final pH. **(D)** Effect of adsorbent content on the adsorption capacities of Cr(VI) by Samples S2 (C$_{Cr(VI)}$ = 100 mg/L, pH = 5, and T = 283 K).

that it can strong respond to UV light and weak respond to visible light. For the Samples S2 and S3, a similar phenomenon could be observed, but the absorption peak shifted to 273 nm and a distinct absorption peak was observed at 456 nm. It is worth noting that the absorption peak intensity of Sample S3 at 456 nm is significantly higher than that of Sample S2, mainly because the absorption peak of Sample S2 is caused by oxygen vacancy or defect, while the Sample S3 is mainly contributed by the interface defect between MgAl$_2$O$_4$ and MgO. (Ewais et al., 2017; Vahid and Haghighi, 2017). According to the results, the Sample S3 has the highest optical absorption coefficient of visible light at the wavelength of 400–620 nm. However, above a wavelength of 620 nm, the Sample S2 has the highest optical absorption coefficient.

According to the UV-Vis absorption spectra and Tauc Equation 4, the Tauc plots of Samples S1-S3 can be obtained.

$$(\alpha E)^n = A\left(E - E_g\right) \tag{4}$$

Where, E = hv, h is Planck's constant, v is the frequency. A and Eg are a constant and the optical band gap of MgAl$_2$O$_4$ nanoparticles, respectively. The Tauc's plots of Samples S1, S2 and S3 as displayed in Figure 5B. The Eg values of Samples S1, S2 and S3 are 3.42, 3.18 and 2.88 V, respectively. The results show that different chelating agents not only have obvious effects on the phase purity and particle size of MgAl$_2$O$_4$, but also have great effects on the optical properties and Eg value of MgAl$_2$O$_4$.
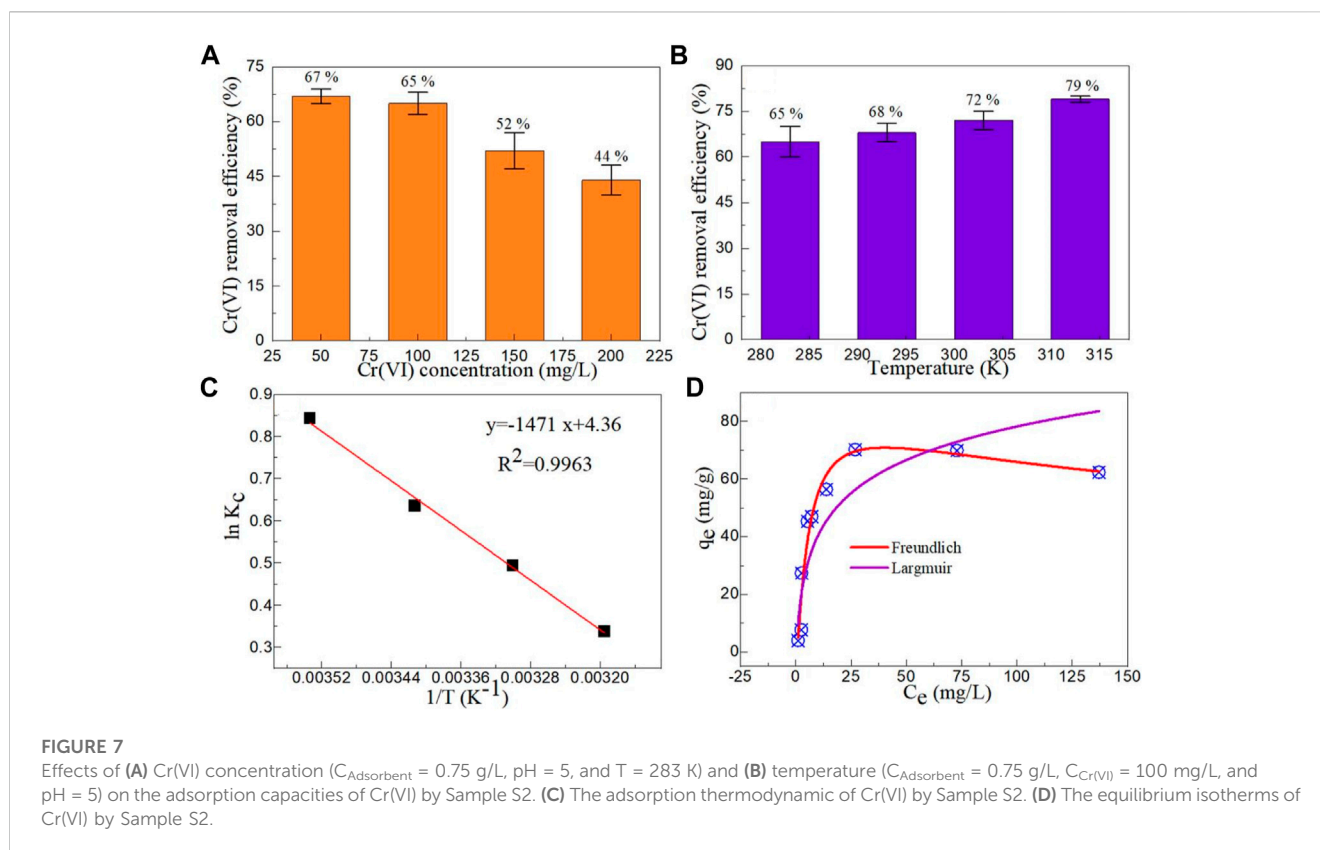
3.4 Adsorption capacity

3.4.1 Effect of adsorption time on the adsorption capacities

MgAl$_2$O$_4$ has been proven to have high adsorption capacity in areas such as dyes and drugs. (Wang et al., 2023; Wang et al., 2023; Wu et al., 2023; Yin et al., 2023). Therefore, it is of great significance to explore the adsorption capacity of MgAl$_2$O$_4$ for adsorption of Cr(VI) ions. Figure 6A depicts the effect of adsorption time on the adsorption capacities of Cr(VI) by Samples S1, S2, and S3. With the increase of adsorption time, the removal efficiency of Cr(VI) from Samples S1, S2, and S3 increased, and the adsorption equilibrium was basically reached after half an hour. Compared with other samples, Sample S2 exhibits the highest Cr (VI) removal efficiency. Combined with the XRD, SEM and TEM analysis, it can be seen that the average particle size of Sample S2 is between Samples S1 and S3, and a small amount of MgO appears in Sample S3, which indicates that MgO has an inhibitory effect on the adsorption capacity of MgAl$_2$O$_4$ to adsorb Cr(VI). Meanwhile, the influence of particle size on the adsorption capacity of MgAl$_2$O$_4$ is not dominant.

3.4.2 Effect of pH value on the adsorption capacities

The initial pH of the reaction solution is one of the key factors affecting the adsorption capacity of MgAl$_2$O$_4$ to adsorb the Cr(VI) ion. Figure 6B shows the effect of pH value on the adsorption capacities of Cr(VI) by Sample S2. According to the experiment, the

FIGURE 7
Effects of **(A)** Cr(VI) concentration ($C_{Adsorbent}$ = 0.75 g/L, pH = 5, and T = 283 K) and **(B)** temperature ($C_{Adsorbent}$ = 0.75 g/L, $C_{Cr(VI)}$ = 100 mg/L, and pH = 5) on the adsorption capacities of Cr(VI) by Sample S2. **(C)** The adsorption thermodynamic of Cr(VI) by Sample S2. **(D)** The equilibrium isotherms of Cr(VI) by Sample S2.

initial pH value of 100 mg/L Cr(VI) solution is 5. Under acidic conditions, the adsorption capacity of $MgAl_2O_4$ is strong, especially when pH = 3, the removal efficiency of Cr(VI) reaches 78%. Under alkaline conditions, the Cr(VI) removal efficiency of $MgAl_2O_4$ is poor. When pH = 13, Cr(VI) removal efficiency is only 38%. Therefore, the $MgAl_2O_4$ nanoparticles showed an obvious acid preference when adsorbing Cr(VI) ions. This is mainly due to the different positive and negative charges on the surface of $MgAl_2O_4$ nanoparticles under different acid-base conditions. Therefore, it is necessary to test the point of zero charge (PZC) of $MgAl_2O_4$ nanoparticles. Figure 6C shows a function of the initial pH and the final pH. It can be seen from the figure that the PZC value of $MgAl_2O_4$ nanoparticles is about 8.97. Villagrán-Olivares et al. (Villagrán-Olivares et al., 2020) reported that the PZC value of $MgAl_2O_4$ nanoparticles is 9.4 ± 0.1. This value is slightly larger than the value obtained in this experiment. When the pH of Cr (VI) solution < PZC value, the surface charge of $MgAl_2O_4$ nanoparticles is positive, and *vice versa*. It can be inferred that the adsorption of Cr(VI) ions by the $MgAl_2O_4$ nanoparticles is mainly electrostatic adsorption.

3.4.3 The effect of initial adsorbent content

The initial content of the adsorbent is another important parameter that affects the adsorption of Cr(VI) by the $MgAl_2O_4$ nanoparticles. Figure 6D displays the effect of adsorbent content on the adsorption capacities of Cr(VI) by Sample S2. With the increase of $MgAl_2O_4$ content, the removal efficiency of Cr(VI) also increases. When the initial content of $MgAl_2O_4$ reached 0.75 mg/L, the removal efficiency of Cr(VI) reached 65%. However, when the

initial content of $MgAl_2O_4$ continued to increase, the removal efficiency of Cr(VI) increased less. This is mainly because the adsorbent content is too high, the adsorbent surface of the active site is not effectively used. (Liu et al., 2014; Kong et al., 2021b). Therefore, the optimal adsorbent content selected by subsequent adsorption and photocatalysis experiments was 0.75 mg/L.

3.4.4 The effect of initial Cr(VI) concentration

The adsorption capacity of $MgAl_2O_4$ nanoparticles is affected by the initial Cr(VI) concentration. Figure 7A shows the effect of Cr(VI) concentration on the adsorption capacities of Cr(VI) by Sample S2. With the increase of the initial concentration of Cr(VI), the removal efficiency of Cr(VI) by the $MgAl_2O_4$ nanoparticles decreased gradually. The main reason for this decline is that the surface active site of a certain amount of $MgAl_2O_4$ nanoparticles is fixed, and continuing to increase the concentration of Cr(VI) will not only make the surface active site not effective use, but also adhere to the surface of the nanoparticles and affect the adsorption of Cr(VI) ions on the surface active site (Bhattacharya et al., 2008; Bhaumik et al., 2011). It is worth noting that the removal efficiency of Cr(VI) at an initial concentration of 100 mg/L is close to that of 50 mg/L. Therefore, the optimal initial concentration of Cr(VI) was chosen to be 100 mg/L.

3.4.5 The effect of temperature

Temperature is also an important parameter that affects the adsorption capacity of the adsorbent. Figure 7B shows the effect of temperature on the adsorption capacities of Cr(VI) by Sample S2. The removal efficiency of Cr(VI) ions by the $MgAl_2O_4$ nanoparticles

increased with the increasing of temperature. The results show that high temperature can improve the adsorption capacity of $MgAl_2O_4$ nanoparticles. At high temperature, the diffusion rate of Cr(VI) ions in $MgAl_2O_4$ nanoparticles is greatly enhanced, which promotes the adsorption of Cr(VI) ions by the $MgAl_2O_4$ nanoparticles. (Ahmad and Kumar, 2010).

According to the experimental results and formulas (5-7), the following parameters such as free energy (ΔG°), enthalpy (ΔH°) and entropy (ΔS°) can be calculated. (Lima et al., 2019).

$$\Delta G^o = -RT \ln K_c \qquad (5)$$

Where, R = 8.314 J/mol/K is the gas constant, T is the temperature, and K_c is the distribution coefficient.

$$K_c = \frac{C_s}{C_e} = \frac{C_0 - C_e}{C_e} \qquad (6)$$

Where, C_s is the concentration in the solid phase (mg/L), C_e is the equilibrium concentration in the supernatant phase (mg/L), and C_0 is the initial adsorbate concentration (mg/L).

$$\ln K_c = \frac{\Delta S^o}{R} - \frac{\Delta H^o}{RT} \qquad (7)$$

According to calculation, Figure 7C shows the adsorption thermodynamic of Cr(VI) by Sample S2. It can be seen that the lnKc and 1/T show excellent linear dependencies. The ΔH° (slope) and ΔS° (intercept) are 1.471 kJ/mol and 4.36 J/mol/K, respectively. According to literature (Kumar et al., 2014), adsorption of Cr(VI) ions by the $MgAl_2O_4$ nanoparticles is an exothermic reaction process. The ΔG° values of $MgAl_2O_4$ nanoparticles at 283, 293, 303 and 313 K are 7.008, 5.286, 4.109 and 2.803 kJ/mol, respectively. The value of ΔG° less than 20 kJ/mol indicates that the adsorption of Cr(VI) ions by the $MgAl_2O_4$ nanoparticles is involved in physical adsorption. This conclusion further confirms that the adsorption of Cr(VI) ions by the $MgAl_2O_4$ nanoparticles is involved in electrostatic adsorption.

To further explore the adsorption capacity of $MgAl_2O_4$ nanoparticles for the adsorption of Cr(VI) ions, different adsorption isothermal models were used to simulate the relevant experimental data. The Freundlich and Langmuir models are two effective models to simulate the adsorption capacity of adsorbents and have potential applications in many fields. The Freundlich and Langmuir models are elaborated by Equations 8 and (9), respectively.

$$q_e = K_F C_e^{\frac{1}{n_F}} \qquad (8)$$

$$q_e = \frac{Q_m K_L C_e}{1 + K_L C_e} \qquad (9)$$

Where, Ce (mg /L) is the equilibrium concentration, Qm (mg/g) is the maximum adsorption capacity, K_L is the Langmuir constant, K_F and n_F are the Freundlich constants. Figure 7D displays the Freundlich and Langmuir models of $MgAl_2O_4$ nanoparticles for the adsorption of Cr(VI) ions. Table 1 shows the parameters of Freundlich and Langmuir models of $MgAl_2O_4$ nanoparticles for the adsorption of Cr(VI) ions. It can be seen from the table that the correlation coefficient of the Freundlich model is close to 1, indicating that the adsorption of Cr(VI) ions by $MgAl_2O_4$ nanoparticles is mainly single-molecule adsorption. The surface

TABLE 1 Parameters of Freundlich and Langmuir models of $MgAl_2O_4$ nanoparticles for the adsorption of Cr(VI) ions.

Models	Parameters	
Freundlich	K_F (mg/g)/(mg/L)^{n_F}	5.131
	n_F	1.659
	R^2	0.99476
Langmuir	Q_m (mg/g)	65.328
	K_L (L/mg)	0.683
	R^2	0.69258

active sites on the surface of $MgAl_2O_4$ nanoparticles have different affinity for Cr(VI) ions, and one Cr(VI) ion may be adsorbed by multiple surface active sites.

3.5 Photocatalytic reduction of Cr(VI)

Although $MgAl_2O_4$ nanoparticles showed excellent adsorption capacity for Cr(VI) ions, the Cr(VI) ions were not completely removed. Further reduction of Cr(VI) ions by the $MgAl_2O_4$ nanoparticles can also be achieved by photoreduction of Cr(VI) ions to Cr(III). Figure 8A shows the time -dependent photoreduction plots of photocatalytic reduction Cr(VI) by Samples S1, S2, and S3. After the adsorption of Cr (VI) ions on Samples S1-S3 reaches adsorption equilibrium, the reaction solution is illuminated, and the concentration of the reaction solution is tested every 10 minutes. It can be seen from the figure that the $MgAl_2O_4$ nanoparticles can effectively reduce Cr(VI) to Cr(III). The ability of $MgAl_2O_4$ nanoparticles to photoreduce Cr(VI) is consistent with its adsorption capacity, and the Sample S2 shows the highest photocatalytic reduction ability.

To gain a more direct insight into the photocatalytic reduction capacity of Samples S1,S2, and S3, the first-order kinetic behavior was used to observe this phenomenon. The first-order kinetic behaviors can be described by the Equation 10.

$$\ln\left(C_t / C_0\right) = -kt \qquad (10)$$

Where, t is the irradiation time, k is the first-order kinetic constant, C_0 is the initial Cr(VI) concentration, C_t is the Cr(VI) concentration at time t. Figure 8B shows the kinetic curves of photocatalytic reduction Cr(VI) by Samples S1, S2, and S3. Through linear fitting with the Origin 2016 software, ln (C_t/C_0) and t show high linear dependence. The k values of photocatalytic reduction Cr(VI) by Samples S1, S2, and S3 as displayed in Figure 8C. The k values of Samples S1, S2, and S3 are 0.02688, 0.05576 and 0.01568 min^{-1}, respectively. The photocatalytic reduction capacity of Sample S2 was 3.56 times that of Sample S3. Figure 8D displays the degradation percentages of photocatalytic reduction Cr(VI) by Samples S1, S2, and S3. The degradation percentages of Samples S1, S2, and S3 are 90%, 99% and 78%, respectively. The results further confirm that the Sample S3 has the best photocatalytic reduction ability. Table 2 shows the photocatalytic reduction ability of AB_2O_4-based photocatalysts toward the photoreduction of Cr(VI) ion. Considering the light source, catalyst
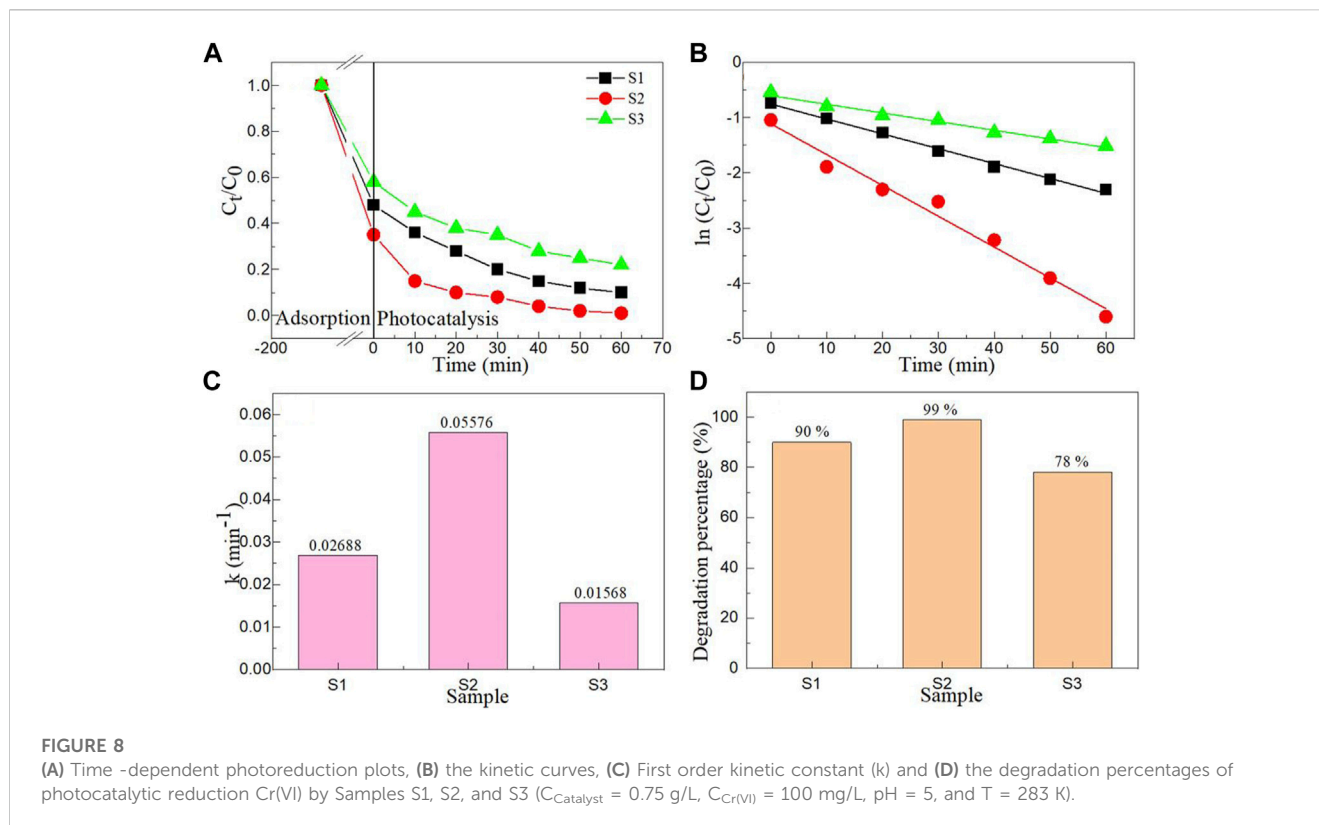
FIGURE 8
(A) Time -dependent photoreduction plots, **(B)** the kinetic curves, **(C)** First order kinetic constant (k) and **(D)** the degradation percentages of photocatalytic reduction Cr(VI) by Samples S1, S2, and S3 ($C_{Catalyst}$ = 0.75 g/L, $C_{Cr(VI)}$ = 100 mg/L, pH = 5, and T = 283 K).

TABLE 2 The photocatalytic reduction ability of AB_2O_4-based photocatalysts toward the photoreduction of Cr(VI) ion.

Samples	Light source	$C_{Catalyst}$ (g L^{-1})	$C_{Cr(VI)}$ (mg/L)	Irradiation time (min)	Degradation percentage (%)	References
$MgAl_2O_4$	150 W Xe lamp	0.75	100	60	99	This work
$NiAl_2O_4$/ZnO	200 W Xe lamp	1	50	300	18	Bouallouche et al. (2019)
$MgCr_2O_4$/WO_3	50 W deuterium lamp	1	30	120	99	Habi Ben Hariz et al. (2022)
$CuAl_2O_4$/TiO_2	200 W tungsten lamp	1	50	180	96	Gherbi et al. (2011), Gherbi et al. (2013)
Cu-doped $ZnAl_2O_4$	700 W/m^2 sunlight	1	1,000	240	79	Akika et al. (2020)
ZnO/$ZnAl_2O_4$	500 W high-pressure Hg lamp	4	150	240	98	Yuan et al. (2018)

content, initial Cr(VI) concentration and irradiation time, the $MgAl_2O_4$ nanoparticles showed the best effect in photocatalytic reduction of Cr(VI) (Gherbi et al., 2011; Gherbi et al., 2013; Yuan et al., 2018; Bouallouche et al., 2019; Akika et al., 2020; Habi Ben Hariz et al., 2022).

The premise of industrial application is that the catalyst can be recycled. Figure 9A shows the cyclic stability experiment of Sample S2 for the photoreduction of Cr(VI) ion. Before each cycle stability experiment, the catalyst in the previous reaction solution should be recovered and centrifuged, filtered, dried and sintered before the next photocatalytic experiment is performed. As can be seen from Figure 9A, after five cycles of experiments, the degradation percentage decreased from 99% to 89%, only by 10%, indicating that the catalyst can be recycled. There are three main reasons for the decrease in degradation percentage: (1) Loss of photocatalyst during use. (2) The active site on

the photocatalyst surface is decreased by continuous adsorption. (3) Continuous adsorption weakens the penetration of incident light.

Capture experiments were performed to gain insight into the role of active species including holes, hydroxyl radicals, superoxide radicals, and electrons in the photocatalysis process. Disodium ethylenediamine tetraacetate (EDTA-2Na, 1 mmol/L), isopropanol (IPA, 1 mmol/L), benzoquinone (BQ, 1 mmol/L), and potassium peroxydisulfate ($K_2S_2O_8$, KSO, 1 mmol/L) were used as the scavengers for holes, hydroxyl radicals, superoxide radicals, and electrons, respectively (Li et al., 2022). When EDTA-2Na, IPA, BQ and KSO were added to the reaction solution, the degradation percentage of Sample S2 was 88%, 76%, 65% and 11%, respectively. The results show that the electrons play an important role in the photocatalytic reduction of Cr(VI) ions by Sample S2.
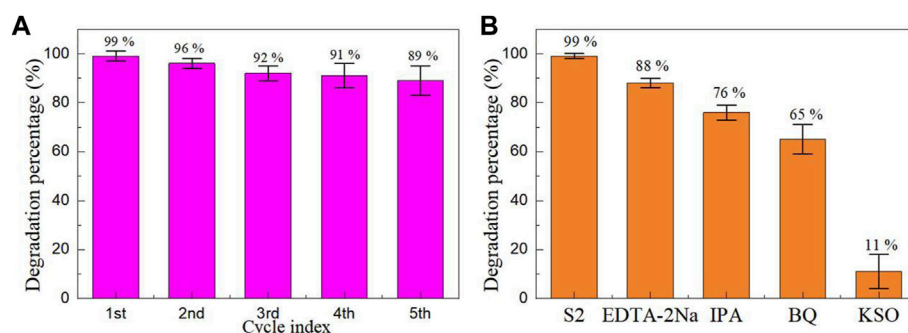
FIGURE 9
(A) Cyclic stability experiment and **(B)** capture experiment of Sample S2 for the photoreduction of Cr(VI) ion.
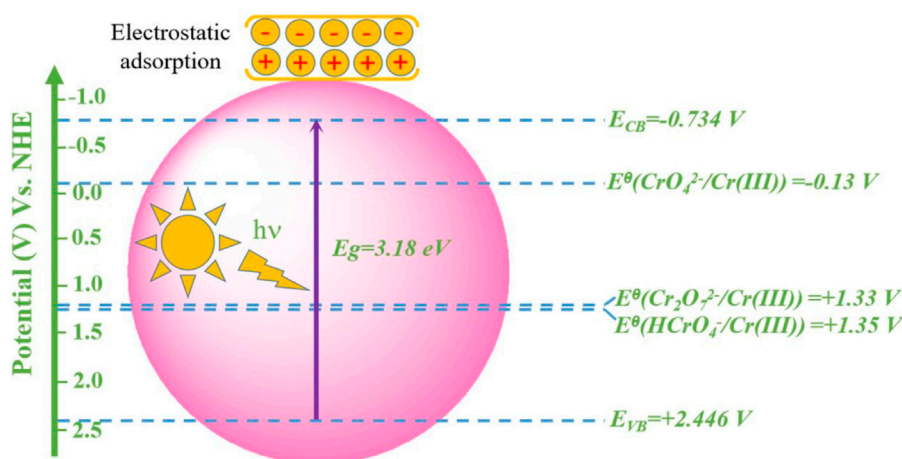

FIGURE 10
Adsorption and photocatalytic mechanisms of MgAl$_2$O$_4$ nanoparticles.

3.6 Adsorption and photocatalytic mechanisms

It can be seen from the adsorption and photocatalytic experiments that the MgAl$_2$O$_4$ nanoparticles have high adsorption and photocatalytic reduction ability. It is found that the adsorption of Cr(VI) ions by the MgAl$_2$O$_4$ nanoparticles is mainly electrostatic adsorption. For the corresponding photocatalytic mechanism, the conduction (E_{CB}) and valence band (E_{VB}) potentials of MgAl$_2$O$_4$ should be calculated by band theory. The E_{CB} = −0.734 V and E_{VB} = 2.446 V of MgAl$_2$O$_4$ can be obtained by Equation 11 and (12).

$$E_{CB} = X - E^e - 0.5E_g \quad (11)$$

$$E_{VB} = X - E^e + 0.5E_g \quad (12)$$

Where, E^e = 4.5 eV, Eg = 3.18 eV and X = 5.356 eV by the following equation:

$$X(MgAl_2O_4) = \sqrt[7]{X(Mg)X(Al)^2X(O)^4} \quad (13)$$

Where, X (Mg) = 3.75 eV, X (Al) = 3.23 eV, and X(O) = 7.54 eV. According to the calculated results, the energy level diagram of MgAl$_2$O$_4$ nanoparticles can be drawn, as shown in Figure 10. Relatively speaking, the MgAl$_2$O$_4$ nanoparticles has a large Eg value, which is difficult to respond to visible light, but the MgAl$_2$O$_4$ nanoparticles contain a certain amount of oxygen vacancies or defects, so that electrons can smoothly transition to its conduction band. The conduction band potential of MgAl$_2$O$_4$ is −0.734 V, which is more negative than E^θ(CrO$_4^{2-}$/Cr^{3+}) = - 0.13 V, so the electrons can participate in a series of reactions to reduce Cr(VI) to Cr(III). (Shi et al., 2020; Li et al., 2022). In addition, the valence band potential of MgAl$_2$O$_4$ is 2.446 V, which is more positive than E^θ(Cr$_2$O$_7^{2-}$/Cr^{3+}) = +1.33 V and E^θ(HCrO$_4$/Cr^{3+}) = +1.35 V, so the holes can produce active radical to reduce Cr(VI) to Cr(III). (Shi et al., 2020; Athira et al., 2021). When there is a small amount of MgO in MgAl$_2$O$_4$, MgO promotes the recombination of electrons and hole pairs in MgAl$_2$O$_4$, which makes the photocatalytic reduction ability of Sample S3 is poor. According to literature (Liu et al., 2014; Wang et al., 2021), the main chemical reactions are as follows:

$$HCrO_4^- + 7H^+ + 3e^- \rightarrow Cr^{3+} + 4H_2O \quad (14)$$

$$Cr^{3+} + 3OH^- \rightarrow Cr(OH)_3\,(s) \quad (15)$$

From the above description, it can be seen that the photocatalytic reduction of Cr(VI) to Cr(III) mainly exists in the form of Cr(OH)$_3$.

4 Conclusion

The MgAl$_2$O$_4$ nanoparticles with the high adsorption capacity and photocatalytic reduction capacity for the adsorption and reduction of Cr(VI) to Cr(III) were fabricated by a conventional polyacrylamide gel route with the different chelating agents including ethylenediamine tetraacetic acid (EDTA), oxalic acid and salicylic acid. When EDTA and oxalic acid were used as chelating agents, pure phase MgAl$_2$O$_4$ nanoparticles were obtained, and oxalic acid was used as chelating agent to introduce defects on the surface of MgAl$_2$O$_4$ nanoparticles. When salicylic acid was used as chelating agent to prepare MgAl$_2$O$_4$ nanoparticles, a small amount of MgO impurities appeared in the sample. The particle surface of all the samples synthesized by chelating agents was approximately spherical, and obvious adhesion agglomeration appeared, and the particle size was 40, 30 and 20 nm successively. Under optimal experimental parameters, the MgAl$_2$O$_4$ nanoparticles synthesized by oxalic acid as chelating agent have higher adsorption and photocatalytic reduction ability than other samples. The high adsorption capacity of the synthesized MgAl$_2$O$_4$ nanoparticles is mainly due to electrostatic adsorption, and the high photocatalytic reduction capacity is mainly due to the active free radical forcing the reduction of Cr(VI) to Cr(III).

Data availability statement

The original contributions presented in the study are included in the article/Supplementary Material, further inquiries can be directed to the corresponding author.

Author contributions

Funding

Conflict of interest

The authors declare that the research was conducted in the absence of any commercial or financial relationships that could be construed as a potential conflict of interest.

Publisher's note

References

Ahmad, R., and Kumar, R. (2010). Adsorptive removal of Congo red dye from aqueous solution using bael shell carbon. *Appl. Surf. Sci.* 257, 1628–1633. doi:10.1016/j.apsusc.2010.08.111

Akika, F. Z., Benamira, M., Lahmar, H., Trari, M., Avramova, I., and Suzer, S. (2020). Structural and optical properties of Cu-doped ZnAl$_2$O$_4$ and its application as photocatalyst for Cr (VI) reduction under sunlight. *Surfaces Interfaces* 18, 100406. doi:10.1016/j.surfin.2019.100406

Athira, T. K., Roshith, M., Babu, T. S., and Kumar, D. V. R. (2021). Fibrous red phosphorus as a non-metallic photocatalyst for the effective reduction of Cr (VI) under direct sunlight. *Mater. Lett.* 283, 128750. doi:10.1016/j.matlet.2020.128750

Bhattacharya, A. K., Naiya, T. K., Mandal, S. N., and Das, S. K. (2008). Adsorption, kinetics and equilibrium studies on removal of Cr (VI) from aqueous solutions using different low-cost adsorbents. *Chem. Eng. J.* 137 (3), 529–541. doi:10.1016/j.cej.2007.05.021

Bhaumik, M., Maity, A., Srinivasu, V. V., and Onyango, M. S. (2011). Enhanced removal of Cr (VI) from aqueous solution using polypyrrole/Fe$_3$O$_4$ magnetic nanocomposite. *J. Hazard. Mater.* 190 (1-3), 381–390. doi:10.1016/j.jhazmat.2011.03.062

Bouallouche, R., Kebir, M., Nasrallah, N., Hachemi, M., and Trari, M. (2019). Enhancement of photocatalytic reduction of Cr(VI) using the hetero-system NiAl$_2$O$_4$/ZnO under visible light. *Algerian J. Environ. Sci. Technol.* 5 (3), 2437–1114.

Budiana, I. G. M. N., Jasman, J., Neolaka, Y. A., Riwu, A. A., Elmsellem, H., Darmokoesoemo, H., et al. (2021). Synthesis, characterization and application of cinnamoyl C-phenylcalix [4] resorcinarene (CCPCR) for removal of Cr (III) ion

from the aquatic environment. *J. Mol. Liq.* 324, 114776. doi:10.1016/j.molliq.2020.114776

Ewais, E. M., El-Amir, A. A., Besisa, D. H., Esmat, M., and El-Anadouli, B. E. (2017). Synthesis of nanocrystalline MgO/MgAl$_2$O$_4$ spinel powders from industrial wastes. *J. Alloys Compd.* 691, 822–833. doi:10.1016/j.jallcom.2016.08.279

Fan, C., Qian, J., Yang, Y., Sun, H., Song, J., and Fan, Y. (2021). Green ceramsite production via calcination of chromium contaminated soil and the toxic Cr (VI) immobilization mechanisms. *J. Clean. Prod.* 315, 128204. doi:10.1016/j.jclepro.2021.128204

Ganesh, I. (2013). A review on magnesium aluminate (MgAl$_2$O$_4$) spinel: synthesis, processing and applications. *Int. Mater. Rev.* 58 (2), 63–112. doi:10.1179/1743280412Y.0000000001

Gao, X., Guo, C., Hao, J., Zhang, Y., Li, M., and Zhao, Z. (2022). Efficient removal of Cr (VI) by modified sodium alginate via synergistic adsorption and photocatalytic reduction. *Appl. Surf. Sci.* 579, 152259. doi:10.1016/j.apsusc.2021.152259

Gherbi, R., Nasrallah, N., Amrane, A., Maachi, R., and Trari, M. (2011). Photocatalytic reduction of Cr(VI) on the new hetero-system CuAl$_2$O$_4$/TiO$_2$. *J. Hazard. Mater.* 186, 1124–1130. doi:10.1016/j.jhazmat.2010.11.105

Gherbi, R., Trari, M., and Nasrallah, N. (2013). Influence of light flux and hydrodynamic flow regime on the photoreduction of Cr (VI) on the CuAl$_2$O$_4$/TiO$_2$ hetero-junction. *J. Environ. Chem. Eng.* 1, 1275–1282. doi:10.1016/j.jece.2013.09.020

Habi Ben Hariz, S., Lahmar, H., Rekhila, G., Bouhala, A., Trari, M., and Benamir, M. (2022). A novel MgCr$_2$O$_4$/WO$_3$ hetero-junction photocatalyst for solar photo reduction

of hexavalent chromium Cr (VI). *J. Photochem. Photobiol. A Chem.* 430, 113986. doi:10.1016/j.jphotochem.2022.113986

Hassanzadeh-Tabrizi, S. A. (2011). Polymer-assisted synthesis and luminescence properties of MgAl₂O₄: tb nanopowder. *Opt. Mater.* 33 (11), 1607–1609. doi:10.1016/j.optmat.2011.04.011

Kong, A., Sun, Y., Peng, M., Gu, H., Fu, Y., Zhang, J., et al. (2021b). Amino-functionalized MXenes for efficient removal of Cr (VI). *Colloids Surfaces A Physicochem. Eng. Aspects* 617, 126388. doi:10.1016/j.colsurfa.2021.126388

Kong, A., Sun, Y., Peng, M., Gu, H., Fu, Y., Zhang, J., et al. (2021a). Amino-functionalized MXenes for efficient removal of Cr (VI). *Colloids Surfaces A Physicochem. Eng. Aspects* 617, 126388. doi:10.1016/j.colsurfa.2021.126388

Kumar, R., Rashid, J., and Barakat, M. A. (2014). Synthesis and characterization of a starch–AlOOH–FeS₂ nanocomposite for the adsorption of Congo red dye from aqueous solution. *RSC Adv.* 4 (72), 38334–38340. doi:10.1039/C4RA05183A

Kumar, V., Dwivedi, S. K., and Oh, S. (2022). A review on microbial-integrated techniques as promising cleaner option for removal of chromium, cadmium and lead from industrial wastewater. *J. Water Process Eng.* 47, 102727. doi:10.1016/j.jwpe.2022.102727

Li, L., Gao, H., Liu, G., Wang, S., Yi, Z., Wu, X., et al. (2022). Synthesis of carnation flower-like Bi2O2CO3 photocatalyst and its promising application for photoreduction of Cr(VI). *Adv. Powder Technol.* 33, 103481. doi:10.1016/j.apt.2022.103481

Li, Q. H., Dong, M., Li, R., Cui, Y. Q., Xie, G. X., Wang, X. X., et al. (2021b). Enhancement of Cr (VI) removal efficiency via adsorption/photocatalysis synergy using electrospun chitosan/g-C₃N₄/TiO₂ nanofibers. *Carbohydr. Polym.* 253, 117200. doi:10.1016/j.carbpol.2020.117200

Li, Y., Gao, Y., Zhang, Q., Wang, R., Li, C., Mao, J., et al. (2021a). Flexible and free-standing pristine polypyrrole membranes with a nanotube structure for repeatable Cr (VI) ion removal. *Sep. Purif. Technol.* 258, 117981. doi:10.1016/j.seppur.2020.117981

Liang, J., Huang, X., Yan, J., Li, Y., Zhao, Z., Liu, Y., et al. (2021). A review of the formation of Cr (VI) via Cr (III) oxidation in soils and groundwater. *Sci. Total Environ.* 774, 145762. doi:10.1016/j.scitotenv.2021.145762

Lima, E. C., Hosseini-Bandegharaei, A., Moreno-Piraján, J. C., and Anastopoulos, I. (2019). A critical review of the estimation of the thermodynamic parameters on adsorption equilibria. Wrong use of equilibrium constant in the Van't Hoof equation for calculation of thermodynamic parameters of adsorption. *J. Mol. Liq.* 273, 425–434. doi:10.1016/j.molliq.2018.10.048

Liu, F., Wang, A., Xiang, M., Hu, Q., and Hu, B. (2022a). Effective adsorption and immobilization of Cr (VI) and U (VI) from aqueous solution by magnetic amine-functionalized SBA-15. *Sep. Purif. Technol.* 282, 120042. doi:10.1016/j.seppur.2021.120042

Liu, F., Xiang, M., Wang, A., Wang, C., and Hu, B. (2021). Efficient adsorption and reduction of Cr (VI) and U (VI) by nanoscale zero-valent iron supported on polydopamine-decorated SBA-15. *Appl. Surf. Sci.* 568, 150931. doi:10.1016/j.apsusc.2021.150931

Liu, H., Wang, S., Gao, H., Yang, H., Wang, F., Chen, X., et al. (2022b). A simple polyacrylamide gel route for the synthesis of MgAl₂O₄ nanoparticles with different metal sources as an efficient adsorbent: neural network algorithm simulation, equilibrium, kinetics and thermodynamic studies. *Sep. Purif. Technol.* 281, 119855. doi:10.1016/j.seppur.2021.119855

Liu, W., Ni, J., and Yin, X. (2014). Synergy of photocatalysis and adsorption for simultaneous removal of Cr (VI) and Cr (III) with TiO₂ and titanate nanotubes. *Water Res.* 53, 12–25. doi:10.1016/j.watres.2013.12.043

Luan, C., Yuan, D., Duan, X., Sun, H., Zhang, G., Guo, S., et al. (2006). Synthesis and characterization of Co²⁺: mgAl₂O₄ nanocrystal. *J. sol-gel Sci. Technol.* 38, 245–249. doi:10.1007/s10971-006-7996-4

Milačič, R., Štupar, J., Kožuh, N., and Korošin, J. (1992). Critical evaluation of three analytical techniques for the determination of chromium (VI) in soil extracts. *Analyst* 117 (2), 125–130. doi:10.1039/AN9921700125

Mukherjee, A., Adak, M. K., Dhak, P., and Dhak, D. (2020). A simple chemical method for the synthesis of Cu²⁺ engrafted MgAl₂O₄ nanoparticles: efficient fluoride adsorbents, photocatalyst and latent fingerprint detection. *J. Environ. Sci.* 88, 301–315. doi:10.1016/j.jes.2019.09.004

Muneeb, M., Ismail, B., Fazal, T., Rehman Khan, A., and Afzia, M. (2016). Adsorption assisted photocatalytic removal of methyl orange by MgAl₂O₄-Sb₂S₃ composite

material. *Recent Pat. Nanotechnol.* 10 (3), 1–220. doi:10.2174/1872210510666161025130344

Nassar, M. Y., Ahmed, I. S., and Samir, I. (2014). A novel synthetic route for magnesium aluminate (MgAl₂O₄) nanoparticles using sol–gel auto combustion method and their photocatalytic properties. *Spectrochim. Acta, Part A.* 131, 329–334. doi:10.1016/j.saa.2014.04.040

Rahmat, N., Yaakob, Z., Pudukudy, M., Rahman, N. A., and Jahaya, S. S. (2018). Single step solid-state fusion for MgAl₂O₄ spinel synthesis and its influence on the structural and textural properties. *Powder Technol.* 329, 409–419. doi:10.1016/j.powtec.2018.02.007

Salmasi, M. Z., Kazemeini, M., Sadjadi, S., and Nematollahi, R. (2022). Spinel MgAl₂O₄ nanospheres coupled with modified graphitic carbon nitride nanosheets as an efficient Z-scheme photocatalyst for photodegradation of organic contaminants. *Appl. Surf. Sci.* 585, 152615. doi:10.1016/j.apsusc.2022.152615

Shi, C., Qi, H., Sun, Z., Qu, K., Huang, Z., Li, J., et al. (2020). Carbon dot-sensitized urchin-like Ti³⁺ self-doped TiO₂ photocatalysts with enhanced photoredox ability for highly efficient removal of Cr⁶⁺ and RhB. *J. Mater. Chem. C* 8 (7), 2238–2247. doi:10.1039/C9TC05513D

Tripathy, S. P., Subudhi, S., Das, S., Ghosh, M. K., Das, M., Acharya, R., et al. (2022). Hydrolytically stable citrate capped Fe₃O₄@ UiO-66-NH₂ mof: A hetero-structure composite with enhanced activity towards Cr (VI) adsorption and photocatalytic H₂ evolution. *J. Colloid Interface Sci.* 606, 353–366. doi:10.1016/j.jcis.2021.08.031

Uddin, M. J., Jeong, Y. K., and Lee, W. (2021). Microbial fuel cells for bioelectricity generation through reduction of hexavalent chromium in wastewater: A review. *Int. J. Hydrogen Energy* 46 (20), 11458–11481. doi:10.1016/j.ijhydene.2020.06.134

Vahid, B. R., and Haghighi, M. (2017). Biodiesel production from sunflower oil over MgO/MgAl₂O₄ nanocatalyst: effect of fuel type on catalyst nanostructure and performance. *Energy Convers. Manag.* 134, 290–300. doi:10.1016/j.enconman.2016.12.048

Villagrán-Olivares, A. C., Gomez, M. F., Barroso, M. N., and Abello, M. C. (2020). Hydrogen production from ethanol: synthesis of Ni catalysts assisted by chelating agents. *Mol. Catal.* 481, 110164. doi:10.1016/j.mcat.2018.08.006

Wang, B., Li, P. Y., Wang, S. Y., Lu, S. H., and Fang, T. (2023b). Tuning the interaction between Pd and MgAl₂O₄ to enhance the dehydrogenation activity and selectivity of dodecahydro-N-ethylcarbazole. *ACS Sustain. Chem. Eng.* 11 (14), 5485–5494. doi:10.1021/acssuschemeng.2c07039

Wang, S., Liu, H., Li, M., Han, M., Gao, H., Yang, H., et al. (2023a). Various carbon-based MgAl₂O₄ adsorbents and their removal efficiency of CR dye and antibiotics in aqueous media: high selective adsorption capacity, performance prediction and mechanism insight. *Ceram. Int.* 49 (16), 26734–26746. doi:10.1016/j.ceramint.2023.05.210

Wang, Y., Lin, N., Gong, Y., Wang, R., and Zhang, X. (2021). Cu–Fe embedded cross-linked 3D hydrogel for enhanced reductive removal of Cr (VI): characterization, performance, and mechanisms. *Chemosphere* 280, 130663. doi:10.1016/j.chemosphere.2021.130663

Wu, Q., Jiang, F., Feng, G., Wang, S., Miao, L., Jiang, W., et al. (2023). Nonhydrolytic sol-gel *in-situ* synthesis of high performance MgAl₂O₄/C adsorbent materials. *Arabian J. Chem.* 16 (3), 104393. doi:10.1016/j.arabjc.2022.104393

Yin, S., López, J. F., Solís, J. J. C., Wong, M. S., and Villagrán, D. (2023). Enhanced adsorption of PFOA with nano MgAl₂O₄@ CNTs: influence of pH and dosage, and environmental conditions. *J. Hazard. Mater. Adv.* 9, 100252. doi:10.1016/j.hazadv.2023.100252

Yuan, X., Cheng, X., Jing, Q., Niu, J., Peng, D., Feng, Z., et al. (2018). ZnO/ZnAl₂O₄ nanocomposite with 3D sphere-like hierarchical structure for photocatalytic reduction of aqueous Cr(VI). *Materials* 11, 1624. doi:10.3390/ma11091624

Zhang, F., Zhang, Y., Wang, Y., Zhu, A., and Zhang, Y. (2022). Efficient photocatalytic reduction of aqueous Cr (VI) by Zr⁴⁺ doped and polyaniline coupled SnS₂ nanoflakes. *Sep. Purif. Technol.* 283, 120161. doi:10.1016/j.seppur.2021.120161

Zhang, J., Yan, M., Sun, G., and Liu, K. (2021). Simultaneous removal of Cu (II), Cd (II), Cr (VI), and rhodamine B in wastewater using TiO₂ nanofibers membrane loaded on porous fly ash ceramic support. *Sep. Purif. Technol.* 272, 118888. doi:10.1016/j.seppur.2021.118888